第43卷第4期
2024年8月

红外与毫米波学报
J. Infrared Millim. Waves

Vol. 43，No. 4
August，2024

**文章编号**：1001-9014(2024)04-0572-10　　**DOI**：**10. 11972/j. issn. 1001-9014. 2024. 04. 018**

# Modified multiple-component scattering power decomposition for PolSAR data based on eigenspace of coherency matrix

ZHANG Shuang[1*]，　WANG Lu[1,2]，　WANG Wen-Qing[1]

（1. School of Automation and Information Engineering，Xi′an University of Technology，Xi'an 710048，China；
2. Ministry of Education Key Lab. of Cognitive Radio and Information Processing，Guilin University of Electronic Technology，Guilin 541004，China）

**Abstract**：A modified multiple-component scattering power decomposition for analyzing polarimetric synthetic aperture radar（PolSAR）data is proposed. The modified decomposition involves two distinct steps. Firstly，eigenvectors of the coherency matrix are used to modify the scattering models. Secondly，the entropy and anisotropy of targets are used to improve the volume scattering power. With the guarantee of high double-bounce scattering power in the urban areas，the proposed algorithm effectively improves the volume scattering power of vegetation areas. The efficacy of the modified multiple-component scattering power decomposition is validated using actual AIRSAR PolSAR data. The scattering power obtained through decomposing the original coherency matrix and the coherency matrix after orientation angle compensation is compared with three algorithms. Results from the experiment demonstrate that the proposed decomposition yields more effective scattering power for different PolSAR data sets.

**Key words**：PolSAR data，model-based decomposition，eigenvalue decomposition，scattering power

# 基于相干矩阵特征空间的改进PolSAR数据多元散射能量分解方法

张　爽[1*]，　王　璐[1,2]，　王文卿[1]

（1. 西安理工大学 自动化与信息工程学院，陕西 西安 710048；
2. 桂林电子科技大学 认知无线电与信息处理省部共建教育部重点实验室，广西 桂林 541004）

**摘要**：文章提出了一种改进的极化合成孔径雷达（PolSAR）数据多元散射能量分解方法。改进后的分解方法包括两个不同的步骤。首先，利用相干矩阵的特征向量对散射模型进行修正；其次，利用目标的熵和各向异性来提高体散射能量。该算法在保持城市区域中较高的二次反射散射能量的前提下，有效地提高了植被区域的体散射能量。利用真实的数据验证了该方法的有效性，将原始相干矩阵分解得到的散射能量和方向角补偿后相干矩阵分解的散射能量与三种已有的分解算法进行了对比。实验结果表明，文章提出的分解方法能够更有效地表示不同地物极化SAR数据集的散射能量。

**关　键　词**：极化SAR数据；模型分解；特征值分解；散射能量

**中图分类号**：TP753　　**文献标识码**：A

## Introduction

Because of all-time，all-weather，and multi-band imaging characteristics，polarimetric synthetic aperture radar（PolSAR）has been widely used in various application areas. In recent years，various new PolSAR sensors have been launched and various PolSAR missions have been carried out，resulting in an increase in the amount of data requiring interpretation and processing. Target decomposition has emerged as the primary approach for

---

**Received date**：2023-09-01，**revised date**：2023-12-05　　**收稿日期**：2023-09-01，**修回日期**：2023-12-05

**Foundation items**：Supported by the National Natural Science Foundation of China（62376214），the Natural Science Basic Research Program of Shaanxi（2023-JC-YB-533），and Foundation of Ministry of Education Key Lab. of Cognitive Radio and Information Processing（Guilin University of Electronic Technology）（CRKL200203）

**Biography**：ZHANG Shuang（1983-），female（Manchu），Liaoning Heishan，lecturer，doctor. Research interests include PolSAR data interpretation and processing，and deep learning application to complex data. E-mail：shzhang_work@163. com

[*] **Corresponding author**：E-mail：shzhang_work@163. com

interpretation and preprocessing due to its ease of implementation and strong physical meaning. For PolSAR images, target decomposition methods can be categorized into two groups: model-based decomposition[1-14] and eigenvalue-based decomposition[15-22].

In 1998, Freeman and Durden introduced the Freeman-Durden decomposition (FDD)[1], which is a classical model-based decomposition method. FDD involves decomposing the covariance matrix of PolSAR data into three main components: surface scattering, double-bounce scattering and volume scattering. Although FDD has efficiently described the physical features of PolSAR data, its major shortcomings are the presence of negative surfaces and double-bounce scattering power. This is due to the assumption of reflection symmetry theory, where the co-polarized term is uncorrelated with the cross-polarized term resulting $T_{13} = 0$ and $T_{23} = 0$ in the coherency matrix $\langle T \rangle$. As a result, the cross-polarized power only contributes to the volume scattering component, causing the volume scattering power to be overestimated and possibly greater than the total power. It leads to negative surfaces and double-bounce scattering powers.

There are three primary methods for enhancing FDD. The first technique involves performing orientation angle compensation (OAC) on the coherency matrix or the covariance matrix of the PolSAR data prior to decomposition[2]. By orienting the coherency or covariance matrix in this way, the cross-polarized power is reduced, resulting in smaller volume scattering power. Consequently, the number of negative surface scattering and double-bounce scattering power is also reduced. The second strategy for improving FDD is to optimize the scattering models, particularly the volume scattering model or by introducing a new scattering model that shares the crossed-polarized power with the volume scattering[5-14]. For example, Yamaguchi introduced the helix scattering model as the fourth component for analysis[5-6], Lamei Zhang et al. proposed a wire scattering model as the fifth component[7], Singh et al. associated $T_{13}$ and $T_{23}$ with physical scattering mechanisms, the six-component scattering decomposition (6SD)[8] and seven-component scattering (7SD)[9] were presented, Wentao An used a modified reflection symmetry decomposition to improve the surface and double-bounce scattering power[10]. The third model-based decomposition methods represent a combination of model-based decomposition and eigenvalue-based decomposition. Cloude made surface and double-bounce scattering models orthogonal to each other, aiming to minimize unknown variables[16]. The orientation angle compensation helps prevent negative values in the scattered power, leading to the popular hybrid Freeman/eigenvalue decomposition technique. Singh et al. enhanced the initial hybrid Freeman/eigenvalue decomposition by utilizing distinct volume scattering models that were scattered from vegetation areas and oriented objects[17].

In this letter, authors present an improved version of multiple component scattering decomposition for PolSAR data. Seven scattering models are used[9], i. e., surface scattering model, double-bounce scattering model, volume scattering model, helix scattering model, oriented dipole scattering model, compound dipole scattering model, and mixed dipole scattering model. Non-negative matrix factorization is achieved by limiting the volume scattered energy to obtain surface scattering and double bounce scattering energy. Additionally, the entropy obtained through eigenvalue decomposition of the coherency matrix enhances the volume scattering power in vegetation areas. The improved version yields non-negative scattering power and outperforms FDD, particularly when applied to vegetation areas.

This letter is organized as follows. The method is presented in Section I, including the proposed scattering model and the improved multiple-component scattering power decomposition. Experimental results on real PolSAR data are compared with several decomposition methods in Section 2, and followed by the conclusions in Section 3.

## 1 Modified scattering decomposition

### 1.1 Scattering models

The multi-look data received in PolSAR systems using the {H, V} basis can be represented as a 3x3 complex matrix, which is also referred to as the coherency matrix. This matrix provides information about the polarization properties of the radar signal, including the phase and amplitude relationships between different polarization components. The coherency matrix of PolSAR image is presented as Eq. (1):

$$\langle T \rangle = \left\langle \vec{k}_p \cdot \vec{k}_p^{*t} \right\rangle = \begin{bmatrix} T_{11} & T_{12} & T_{13} \\ T_{12}^* & T_{22} & T_{23} \\ T_{13}^* & T_{23}^* & T_{33} \end{bmatrix} . \quad (1)$$

In the PolSAR systems, $\vec{k}_\mathrm{p}$ is a Pauli vector representing single-look data. The angle brackets $\langle \cdot \rangle$ denote the mean of several observations from the objects within a resolution cell. As a result, $\langle T \rangle$ is a positive semidefinite Hermitian matrix.

Freeman and Durden developed the technique for PolSAR systems to break down the covariance matrix or the coherency matrix into three separate components. These three components consist of the surface scattering component, double-bounce scattering component, and volume scattering component[1]. Gulab Singh and his colleagues attributed physical scattering mechanisms to $T_{23}$ and $T_{13}$, and established seven-component scattering decomposition (7SD) to provide an explanation for the coherency matrix of PolSAR data[9]. The scattering decomposition in this letter is demonstrated on the coherency matrix, and the coherency matrix is divided into seven parts as follows[9]:

$$\begin{aligned} \langle T \rangle = m_\mathrm{s} T_\mathrm{s} + m_\mathrm{d} T_\mathrm{d} + m_\mathrm{v} T_\mathrm{v} + m_\mathrm{h} T_\mathrm{h} + m_\mathrm{md} T_\mathrm{md} \\ + m_\mathrm{cd} T_\mathrm{cd} + m_\mathrm{od} T_{od} \end{aligned} , \quad (2)$$

where $T_\mathrm{s}$, $T_\mathrm{d}$, $T_\mathrm{v}$, $T_\mathrm{h}$, $T_\mathrm{md}$, $T_\mathrm{cd}$ and $T_\mathrm{od}$ denote surface scattering model, double-bounce scattering model, volume scattering model, helix scattering model, oriented dipole scattering model, compound dipole scattering model, and mixed dipole scattering model respectively.

Correspondingly, $m_s$, $m_d$, $m_v$, $m_h$, $m_{md}$, $m_{cd}$, and $m_{od}$ represent the corresponding scattering power of the seven scattering models.

$T_s$, $T_d$, $T_v$, $T_h$, $T_{md}$, $T_{cd}$ and $T_{od}$ are shown as follows[9]:

$$T_s = \frac{1}{|\beta|^2 + 1}\begin{bmatrix} 1 & \beta^* & 0 \\ \beta & |\beta|^2 & 0 \\ 0 & 0 & 0 \end{bmatrix} \quad , \quad (3)$$

$$T_d = \frac{1}{|\alpha|^2 + 1}\begin{bmatrix} |\alpha|^2 & \alpha & 0 \\ \alpha^* & 1 & 0 \\ 0 & 0 & 0 \end{bmatrix} \quad , \quad (4)$$

$$T_v = \frac{1}{4}\begin{bmatrix} 4 & 0 & 0 \\ 0 & 1 & 0 \\ 0 & 0 & 1 \end{bmatrix} \quad , \quad (5a)$$

$$T_v = \frac{1}{30}\begin{bmatrix} 15 & -5 & 0 \\ -5 & 7 & 0 \\ 0 & 0 & 8 \end{bmatrix} \quad , \quad (5b)$$

$$T_v = \frac{1}{30}\begin{bmatrix} 15 & 5 & 0 \\ 5 & 7 & 0 \\ 0 & 0 & 8 \end{bmatrix} \quad , \quad (5c)$$

$$T_v = \frac{1}{15}\begin{bmatrix} 0 & 0 & 0 \\ 0 & 7 & 0 \\ 0 & 0 & 8 \end{bmatrix} \quad , \quad (5d)$$

$$T_h = \frac{1}{2}\begin{bmatrix} 0 & 0 & 0 \\ 0 & 1 & \mp j \\ 0 & \pm j & 1 \end{bmatrix} \quad , \quad (6)$$

$$T_{md} = \frac{1}{2}\begin{bmatrix} 0 & 0 & 0 \\ 0 & 1 & \pm 1 \\ 0 & \pm 1 & 1 \end{bmatrix} \quad , \quad (7)$$

$$T_{cd} = \frac{1}{2}\begin{bmatrix} 1 & 0 & \pm j \\ 0 & 0 & 0 \\ \mp j & 0 & 1 \end{bmatrix} \quad , \quad (8)$$

$$T_{od} = \frac{1}{2}\begin{bmatrix} 1 & 0 & \pm 1 \\ 0 & 0 & 0 \\ \pm 1 & 0 & 1 \end{bmatrix} \quad , \quad (9)$$

where coefficient $\beta$ in Eq. (3) sets $0 < \beta < 1$ and a in Eq. (4) is a complex value with $|\alpha| < 1$. $T_v$ in Eqs. (5a), (5b), (5c) and (5d) is the volume scattering model under different cases. $j$ represents an imaginary number.

## 1.2 Modified decomposition

This part presents an improved multiple component scattering decomposition for PolSAR data based on entropy $H$ and anisotropy $A$. These two parameters are used to enhance the volume scattering power in vegetation areas with high-entropy. PolSAR data are divided into two categories: vegetation areas with high-entropy and other areas. Different decomposition techniques are adopted to obtain better scattering power. The volume scattering power in vegetation areas has been improved while ensuring good performance in other areas.

According to the decomposition formula in Eq. (2) above and the model in Eqs. (3)-(9), $m_h$ and $m_{md}$ can be calculated from $T_{23}$, while $m_{cd}$ and $m_{od}$ can be calculated from $T_{13}$. The solutions are shown as:

$$m_h = 2\left|\mathrm{Im}(T_{23})\right| \quad , \quad (10)$$

$$m_{md} = 2\left|\mathrm{Re}(T_{23})\right| \quad , \quad (11)$$

$$m_{cd} = 2\left|\mathrm{Im}(T_{13})\right| \quad , \quad (12)$$

$$m_{od} = 2\left|\mathrm{Re}(T_{13})\right| \quad , \quad (13)$$

where Im() in Eqs. (10) and (12) denotes the process of extracting the imaginary part of an element and Re() in Eqs. (11) and (13) denotes the process of extracting the real part of an element.

After removing the four scattering power mentioned above from the coherency matrix, the residual part contains surface scattering power, double-bounce scattering power, and volume scattering power as shown in Eq. (14), with the residual part $\langle T^{re} \rangle$ shown in Eq. (15):

$$\begin{aligned} \langle T^{re} \rangle &= m_s T_s + m_d T_d + m_v T_v \\ &= \langle T \rangle - m_h T_h - m_{md} T_{md} - m_{cd} T_{cd} - m_{od} T_{od} \quad , \quad (14) \end{aligned}$$

$$\langle T^{re} \rangle = \begin{bmatrix} T_{11}^{re} & T_{12}^{re} & T_{13}^{re} \\ T_{12}^{re*} & T_{22}^{re} & T_{23}^{re} \\ T_{13}^{re*} & T_{23}^{re*} & T_{33}^{re} \end{bmatrix} \quad . \quad (15)$$

Each element in $T_{re}$ is represented as follows:

$$T_{11}^{re} = T_{11} - \frac{1}{2}m_{cd} - \frac{1}{2}m_{od} = T_{11} - \left|\mathrm{Im}\left(T_{13}\right)\right| - \left|\mathrm{Re}(T_{13})\right| \quad , \quad (16)$$

$$T_{22}^{re} = T_{22} - \frac{1}{2}m_h - \frac{1}{2}m_{md} = T_{22} - \left|\mathrm{Im}\left(T_{23}\right)\right| - \left|\mathrm{Re}(T_{23})\right| \quad , \quad (17)$$

$$\begin{aligned} T_{33}^{re} &= T_{33} - \frac{1}{2}m_h - \frac{1}{2}m_{md} - \frac{1}{2}m_{cd} - \frac{1}{2}m_{od} \\ &= T_{33} - \left|\mathrm{Im}\left(T_{23}\right)\right| - \left|\mathrm{Re}(T_{23})\right| - \left|\mathrm{Im}\left(T_{13}\right)\right| - \left|\mathrm{Re}(T_{13})\right| \quad , \quad (18) \end{aligned}$$

$$T_{12}^{re} = T_{12} \quad , \quad (19)$$

$$\begin{aligned} T_{13}^{re} &= T_{13} \pm \frac{1}{2}m_{cd} j \pm \frac{1}{2}m_{od} \\ &= T_{13} - \mathrm{Im}\left(T_{13}\right)j - \mathrm{Re}\left(T_{13}\right) = 0 \quad , \quad (20) \end{aligned}$$

$$\begin{aligned} T_{23}^{re} &= T_{23} \mp \frac{1}{2}m_h j \pm \frac{1}{2}m_{md} \\ &= T_{23} - \mathrm{Im}\left(T_{23}\right)j - \mathrm{Re}(T_{23}) = 0 \quad . \quad (21) \end{aligned}$$

To ensure that the three scattering power, i. e., $m_s$, $m_d$ and $m_v$ from $\langle T^{re} \rangle$ is positive, it is necessary to ensure that $T_{11}^{re}$, $T_{22}^{re}$ and $T_{33}^{re}$ are all positive. However, there may be certain pixels where these values are less than zero. In these instances, $m_h$, $m_{md}$, $m_{cd}$, and $m_{od}$ must be modified appropriately to ensure that $T_{11}^{re}$, $T_{22}^{re}$ and $T_{33}^{re}$ remain non-negative. If $T_{33}^{re}<0$, gradually reduce $m_h$, $m_{md}$, $m_{cd}$, and $m_{od}$ at the same time until $T_{33}^{re}>=0$ is satisfied. Then, if $T_{11}^{re}$ is still less than 0, set $m_{cd} = 0$ and $m_{od} = 0$. Similarly, if $T_{22}^{re}$ is still less than 0, set $m_h = 0$ and $m_{md} = 0$.

After obtaining the values of $m_h$, $m_{md}$, $m_{cd}$, and $m_{od}$ through the above solution, in order to calculate the value of $m_s$, $m_d$ and $m_v$, $T_{13}^{re}$ and $T_{23}^{re}$ which are not equal to 0 in some pixels are ignored, and the residual matrix $\langle T^{re} \rangle$ is set to the following form as Eqs. (22) and (23):

$$\langle T^{re} \rangle = \begin{bmatrix} T_{11}^{re} & T_{12}^{re} & 0 \\ T_{12}^{re*} & T_{22}^{re} & 0 \\ 0 & 0 & T_{33}^{re} \end{bmatrix} \quad , \quad (22)$$

$$\langle T^{re} \rangle = m_s T_s + m_d T_d + m_v T_v \quad . \quad (23)$$

To determine the volume scattering power $m_v$, it is first necessary to determine whether the volume scattering is from the dihedral structure or the dipole structure. Set $C_1 = T_{11}^{re} - T_{22}^{re}$, such that if $C_1 < 0$, the volume scattering model $T_v$ is shown as Eq. (5d), and if $C_1 \geqslant 0$, the volume scattering model $T_v$ is shown as one of Eqs. (5a), (5b) and (5c). By utilizing the co-polarized ratio $R$ of Eq. (24), one can determine the suitable model for the volume scattering. The detailed steps are as follows: if $|R| \leqslant 2$, the volume scattering model $T_v$ is shown as Eq. (5a); if $R > 2$, $T_v$ is shown as Eq. (5b); if $R < -2$, $T_v$ is shown as Eq. (5c)[3]. The solutions for the volume scattering power $m_v$ under various scenarios are expressed as Eq. (25):

$$R = 10\log\left(\frac{|S_{VV}|^2}{|S_{HH}|^2}\right) = 10\log\left(\frac{T_{11}^{re} + T_{22}^{re} - 2\mathrm{Re}(T_{12}^{re})}{T_{11}^{re} + T_{22}^{re} + 2\mathrm{Re}(T_{12}^{re})}\right), \quad (24)$$

$$m_v = \begin{cases} 4T_{33}^{re} & if\left(T_{11}^{re} - T_{22}^{re}\right) \geqslant 0 \ and \ |R| \leqslant 2 \\ \frac{30}{8}T_{33}^{re} & if\left(T_{11}^{re} - T_{22}^{re}\right) \geqslant 0 \ and \ R > 2 \\ \frac{30}{8}T_{33}^{re} & if\left(T_{11}^{re} - T_{22}^{re}\right) \geqslant 0 \ and \ R < -2 \\ \frac{15}{8}T_{33}^{re} & if\left(T_{11}^{re} - T_{22}^{re}\right) < 0 \end{cases} . \quad (25)$$

After subtracting the volume scattering part from $\langle T^{re}\rangle$ denoted by $\langle T^{sd}\rangle$ as shown in Eq. (26), $\langle T^{sd}\rangle$ consists of surface scattering part and double-bounce scattering part and the different cases of the volume scattering part are shown in Eq. (27):

$$\langle T^{sd}\rangle = m_s T_s + m_d T_d = \langle T^{re}\rangle - m_v T_v = \begin{bmatrix} T_{11}^{sd} & T_{12}^{sd} & 0 \\ T_{12}^{sd*} & T_{22}^{sd} & 0 \\ 0 & 0 & 0 \end{bmatrix}, \quad (26)$$

$$\langle T^{sd}\rangle = \begin{cases} \begin{bmatrix} T_{11}^{re} - \frac{1}{2}m_v & T_{12}^{re} & 0 \\ T_{12}^{re*} & T_{22}^{re} - \frac{1}{4}m_v & 0 \\ 0 & 0 & 0 \end{bmatrix} & \text{if } T_v \text{ is (5a)} \\ \begin{bmatrix} T_{11}^{re} - \frac{1}{2}m_v & T_{12}^{re} + \frac{1}{6}m_v & 0 \\ T_{12}^{re*} + \frac{1}{6}m_v & T_{22}^{re} - \frac{7}{8}m_v & 0 \\ 0 & 0 & 0 \end{bmatrix} & \text{if } T_v \text{ is (5b)} \\ \begin{bmatrix} T_{11}^{re} - \frac{1}{2}m_v & T_{12}^{re} - \frac{1}{6}m_v & 0 \\ T_{12}^{re*} - \frac{1}{6}m_v & T_{22}^{re} - \frac{7}{8}m_v & 0 \\ 0 & 0 & 0 \end{bmatrix} & \text{if } T_v \text{ is (5c)} \\ \begin{bmatrix} T_{11}^{re} & T_{12}^{re} & 0 \\ T_{12}^{re*} & T_{22}^{re} - \frac{7}{8}m_v & 0 \\ 0 & 0 & 0 \end{bmatrix} & \text{if } T_v \text{ is (5d)} \end{cases} . \quad (27)$$

The volume scattering power $m_v$ is represented as Eq. (25), while the surface scattering power $m_s$ and double-bounce scattering power $m_d$ are the eigenvalues of $\langle T^{sd}\rangle$. The eigenvalue decomposition of $\langle T^{sd}\rangle$ is shown as Eq. (28):

$$\langle T^{sd}\rangle = \lambda_1 k_1{}^* k_1^t + \lambda_2 k_2{}^* k_2^t \quad , \quad (28)$$

$$k_i = \begin{bmatrix} \cos\alpha_i \\ \sin\alpha_i \cos\beta_i e^{j\delta_i} \\ 0 \end{bmatrix} \quad , \quad (29)$$

where $\lambda_1$ and $\lambda_2$ are the eigenvalues, and $k_1$ and $k_2$ are the corresponding eigenvectors as shown in Eq. (29) with $\alpha_1 + \alpha_2 = 90^\circ$. According to Ref. [17], when the sum of scattering mechanism angles $\alpha_1 + \alpha_2 = 90^\circ$, it can be considered that the surface scattering model and the double-bounce scattering model are derived from the eigenvector space of the coherency matrix. The specific situations are as follows: if $\alpha_1 \leqslant 45^\circ$, then $T_s = k_1{}^* k_1^t$ and $T_d = k_2{}^* k_2^t$; if $\alpha_1 > 45^\circ$, then $T_s = k_2{}^* k_2^t$, and $T_d = k_1{}^* k_1^t$. The surface scattering power $m_s$ and double-bounce scattering power $m_d$ can be solved as Eq. (30):

$$\begin{cases} m_s = \lambda_1 \\ m_d = \lambda_2 \end{cases} \text{If } \alpha_1 \leqslant 45^\circ \qquad \begin{cases} m_s = \lambda_2 \\ m_d = \lambda_1 \end{cases} \text{If } \alpha_1 > 45^\circ \quad . \quad (30)$$

In cases where $\lambda_1$ or $\lambda_2$ of $\langle T^{sd}\rangle$ is less than zero, the volume scattering power $m_v$ can be gradually reduced until $\lambda_1 \geqslant 0$ and $\lambda_2 \geqslant 0$ conditions are met. Subsequently, surface scattering power $m_s$ and double-bounce scattering power $m_d$ can be calculated using Eq. (30).

To ensure non-negative eigenvalues $\lambda_1$ and $\lambda_2$, the volume scattering power $m_v$ is typically reduced, often leading to an underestimation of $m_v$, especially in high-entropy regions. To address this issue, adjustments are made to the calculation method for volume scattering power $m_v$ in high-entropy regions. It is considered that $\langle T^{sd}\rangle$ of high-entropy regions comprises the double-bounce scattering and the volume scattering, with the surface scattering excluded.

Entropy of the coherency matrix is calculated as Eq. (31)[15]. $p_i$ in Eq. (32) is the normalized eigenvalue $\lambda_i$ of the coherency matrix $\langle T\rangle$. Entropy represents the degree of randomness of the targets in a cell. When entropy is equal to 1, it means that the current target is completely random and usually belongs to the vegetation areas. When entropy equals zero, it means that the target is not random at all and is a deterministic target, which usually belongs to the rough surface areas.

$$H = -\sum_{i=1}^{3} p_i \cdot \log_3 p_i \quad , \quad (31)$$

$$p_i = \frac{\lambda_i}{\lambda_1 + \lambda_2 + \lambda_3}, \ i \in \{1, 2, 3\} \quad , \quad (32)$$

$$A = \frac{\lambda_2 - \lambda_3}{\lambda_2 + \lambda_3} \quad . \quad (33)$$

Anisotropy $A$ in Eq. (33) indicates the degree of heterogeneity of the target. In PolSAR images, anisotropy $A$ is often paired with entropy $H$[15]. When the entropy $H$ is high, anisotropy $A$ helps differentiate between targets in vegetation areas and artificial ones. Additionally, besides the volume scattering power $m_v$ calculated in Eq. (25), it is believed that part of volume scattering power exists in the matrix $\langle T^{sd}\rangle$ in some high-entropy case. When $H - A > 0.4$, the target is considered to be the vegetation area, and the calculation of $m_s$, $m_d$, and the additional $m_v$ is as follows:

$$\begin{cases} \begin{cases} m_s = 0 \\ m_d = \lambda_2 \quad \text{If}\ \alpha_1 \leqslant 50^{\circ} \\ m_v = \lambda_1 \end{cases} \\ \begin{cases} m_s = 0 \\ m_d = \lambda_1 \quad \text{If}\ \alpha_1 > 50^{\circ} \\ m_v = \lambda_2 \end{cases} \end{cases} \text{if } H - A > 0.4 \quad . \qquad (34)$$

The flowchart of the modified multiple-component scattering power decomposition for the original coherency matrix of the PolSAR data is depicted in Fig. 1.

In this letter, the orientation angle compensation (OAC) can be applied to the modified decomposition method. The rotation matrices are presented in Eqs. (35) and (36). The coherency matrices are shown as Eqs. (37) and (38) after two OACs. To minimize $T_{33}$ and $T_{33}(\theta)$, the values of $\theta$ and $\varphi$ can be determined as illustrated in Eqs. (39) and (40) respectively:

$$R(\theta) = \begin{bmatrix} 1 & 0 & 0 \\ 0 & \cos 2\theta & \sin 2\theta \\ 0 & -\sin 2\theta & \cos 2\theta \end{bmatrix} \quad , \qquad (35)$$

$$U(\varphi) = \begin{bmatrix} 1 & 0 & 0 \\ 0 & \cos 2\varphi & j\sin 2\varphi \\ 0 & j\sin 2\varphi & \cos 2\varphi \end{bmatrix} \quad , \qquad (36)$$

$$\langle T(\theta) \rangle = R(\theta) \langle T \rangle R(\theta)' \quad , \qquad (37)$$

$$\langle T(\varphi) \rangle = U(\varphi) \langle T(\theta) \rangle U(\varphi)' \quad , \qquad (38)$$

$$\theta = \frac{1}{4} \tan^{-1}\left( \frac{2\,\mathrm{Re}(T_{23})}{T_{22} - T_{33}} \right) + \frac{n\pi}{4}, \quad n = 0, \pm 1 , \qquad (39)$$

$$\varphi = \frac{1}{4} \tan^{-1}\left( \frac{2\,\mathrm{Im}(T_{23}(\theta))}{T_{22}(\theta) - T_{33}(\theta)} \right) + \frac{m\pi}{4}, \quad m = 0, \pm 1 . \qquad (40)$$

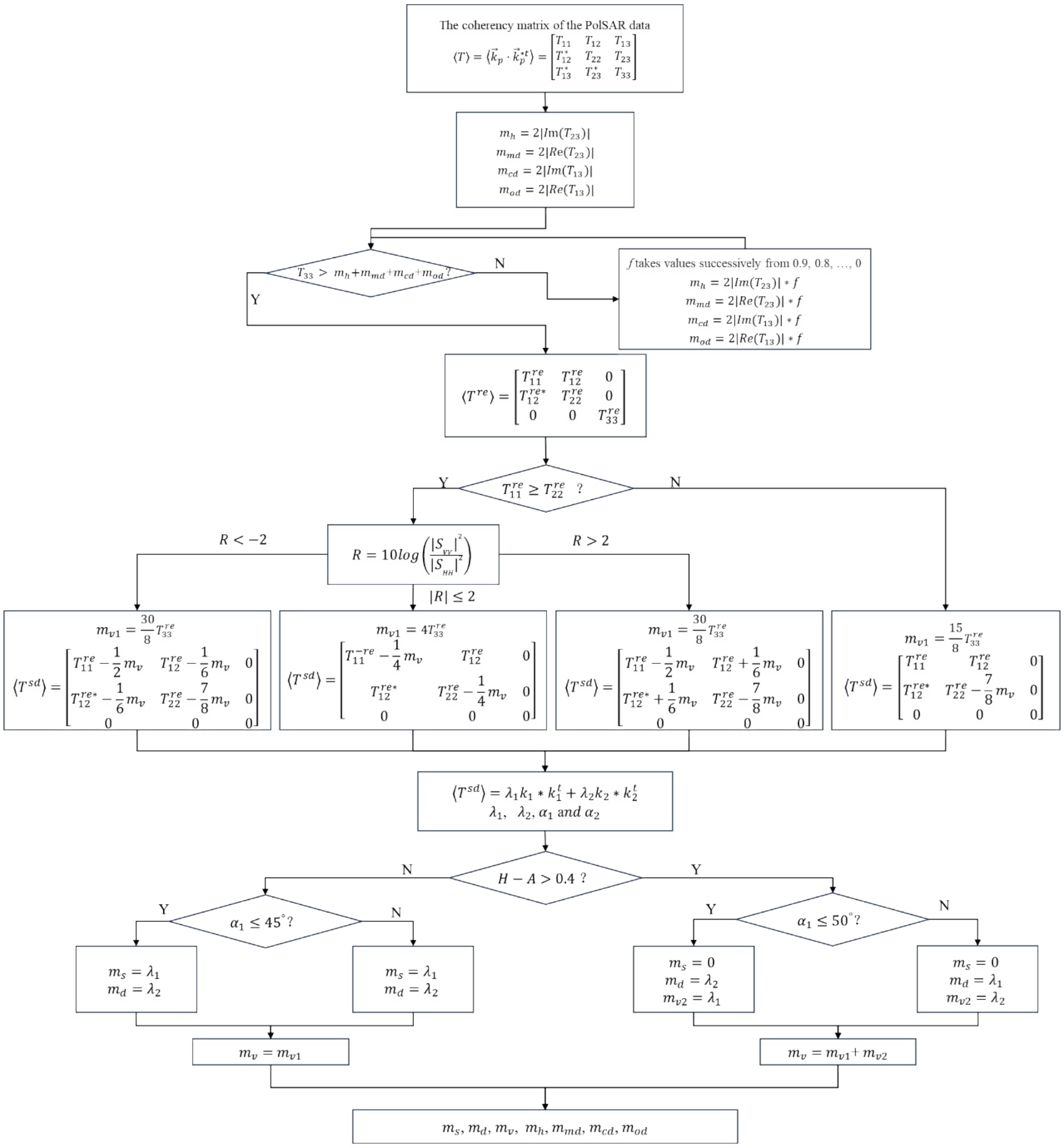

Fig. 1 Flowchart of modified multiple-component scattering power decomposition
图1 改进的多元散射能量分解方法流程图

After the first OAC by $R(\theta)$, $\mathrm{Re}\left(T_{23}(\theta)\right)=0$, as per Eq. (11), $m_{\mathrm{md}}=0$. The proposed method evolves into a six-component scattering power decomposition. Following the second OAC by $U(\varphi)$, $T_{23}(\varphi)=0$, as per Eq. (10), $m_{\mathrm{h}}=0$. Consequently, the proposed method transforms into a five-component scattering power decomposition.

## 2 Experimental results

To demonstrate the effectiveness of the proposed multiple-component scattering power decomposition for PolSAR data based on eigenspace of coherency matrix, various experiments were conducted using fully PolSAR data. An L-band 4-look AIRSAR dataset covering San Francisco is utilized. It has a resolution of 10 m×10 m, with the radar incidence angles ranging from 5° to 60°, and the selected image size is 700×600 pixels. The data is in the $\{H, V\}$ base, and the diagonal elements of the coherency matrix form a color image with $T_{11}$ representing blue, $T_{22}$ representing red, and $T_{33}$ representing green, as shown in Fig. 2. Three areas outlined by red rectangles in Fig. 2 are designated for subsequent experimental demonstrations, labeled as zone1, zone2, and zone3 from top to bottom. The respective terrain labels for zone1, zone2, and zone3 are ocean areas, urban areas and vegetation areas.

Three decomposition algorithms are selected to compare and demonstrate the results of the proposed decomposition (PD) in this letter, including the Freeman-Durden scattering power decomposition (FDD)[1] utilizing three volume scattering models (volume scattering models are shown in Eqs. (5a), (5b), and (5c)), Yamaguchi four-component scattering power decomposition (Y4D)[3], seven-component scattering power decomposition (7SD)[9]. Figures 3-5 display the decomposition results of the AIRSAR data. In these figures, surface scattering power $m_{\mathrm{s}}$ is represented in blue, double-bounce scattering power $m_{\mathrm{d}}$ in red, and volume scattering power $m_{\mathrm{v}}$ in green. Figure 3 presents the decomposition results of the original coherency matrix of the AIRSAR data without OAC. Figure 4 shows the decomposition results of the coherency matrix with the OAC applied using $R(\theta)$. Figure 5 illustrates the decomposition results of the coherency matrix with two types of OAC applied sequentially using $R(\theta)$ and $U(\varphi)$.

Fig. 2 Original image
图2 原图

As shown in Figs. 3-5, the four decomposition algorithms effectively preserve the key features of the AIRSAR data by extracting the three main scattering power $m_{\mathrm{s}}$, $m_{\mathrm{d}}$, and $m_{\mathrm{v}}$. In Fig. 3(c), Fig. 4(c), and Fig. 5(c), 7SD demonstrates superior performance in urban areas, with colors leaning towards red. This suggests a higher concentration of double-bounce scattering power in these areas. In contrast, in Fig. 3(d), Fig. 4(d), and Fig. 5(d), PD exhibits a reddish tint for urban areas, indicating a significant presence of double-bounce scattering power. Vegetation areas show a tendency towards green, indicating a higher proportion of volume scattering power in these regions.

To visually demonstrate the effectiveness of the proposed algorithm in scattering power, the scattering power of the original coherency matrix of the AIRSAR data without OAC are represented in Figs. 6-8. The scattering power is shown as a grayscale image, where black indicates a 0% proportion and white indicates a 100% propor-

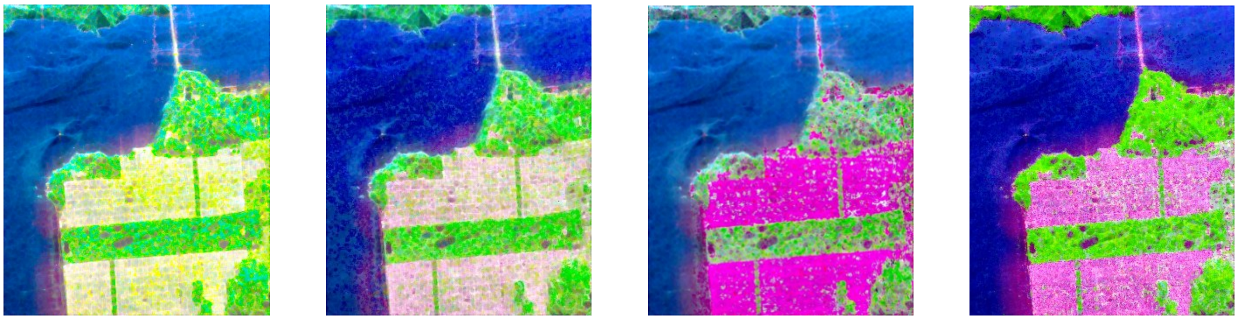

(a) FDD (b) Y4D (c) 7SD (d) PD

Fig. 3 Decomposition results for the coherency matrix
图3 相干矩阵的分解结果

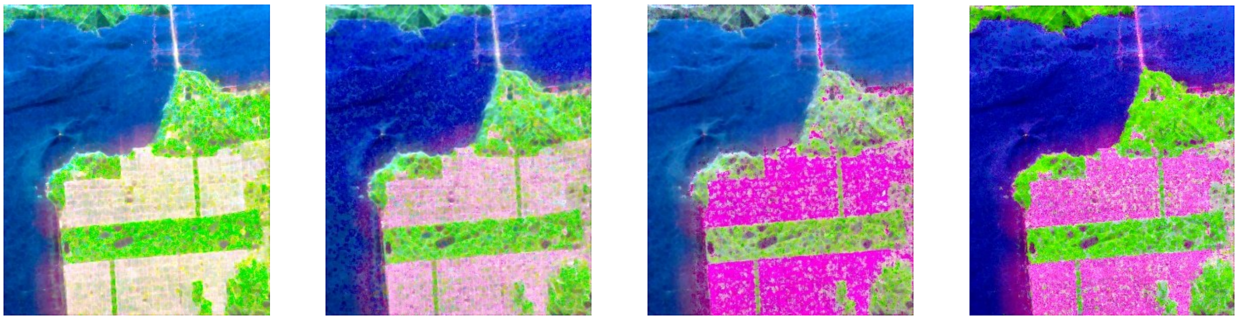

（a）FDD （b）Y4D （c）7SD （d）PD

Fig. 4 Decomposition results for the coherency matrix with OAC by $R(\theta)$
图4 $R(\theta)$方位角补偿后相干矩阵的分解结果

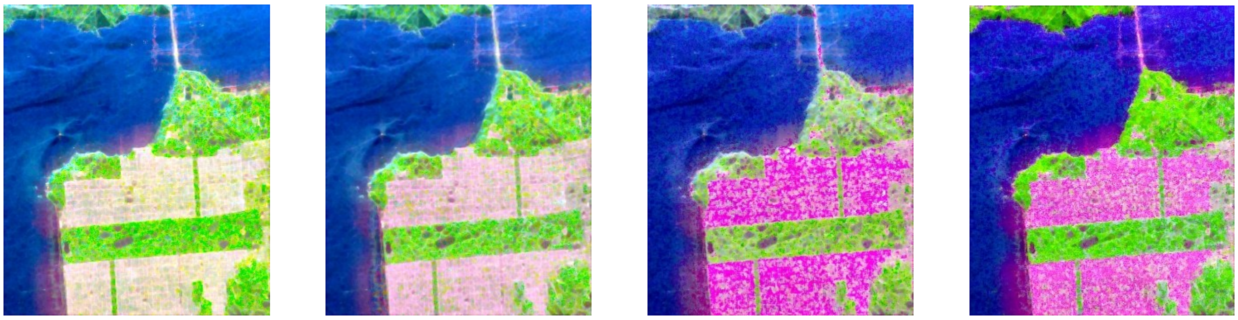

（a）FDD （b）Y4D （c）7SD （d）PD

Fig. 5 Decomposition results for the coherency matrix with OAC by $R(\theta)$ and $U(\varphi)$
图5 $R(\theta)$和$U(\varphi)$方位角补偿后相干矩阵的分解结果

tion in terms of total power. Based on Figs. 6-8, it can be concluded that all four decomposition algorithms can obtain higher surface scattering power over ocean areas, the double-bounce scattering power is strongest in urban areas and volume scattering power is strongest in vegetation areas. In Fig. 8, PD not only ensures the largest volume scattering power of vegetation areas but also minimizes the volume scattering power in urban areas and ocean areas.

Quantitative comparison is made using the three zones in Fig. 2. The scattering power from these decomposition algorithms for the original coherency matrices without OAC in zone1, zone2, and zone3 is displayed in Tables 1-3, respectively.

From Tables 1-3, it can be observed that, compared with the other three algorithms, the proportion of surface scattering power of PD algorithm in zone1 is as high as 93.64%, only slightly inferior to Y4D. In

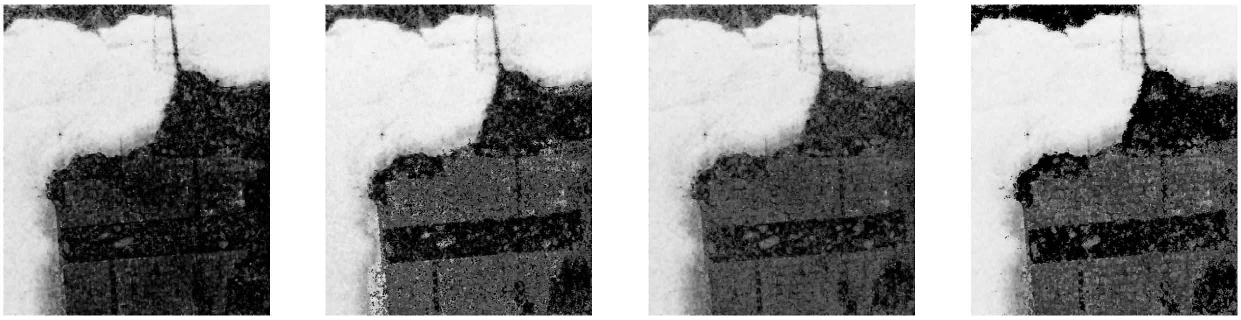

（a）FDD （b）Y4D （c）7SD （d）PD

Fig. 6 Surface scattering power of the coherency matrix
图6 相干矩阵的表面散射能量

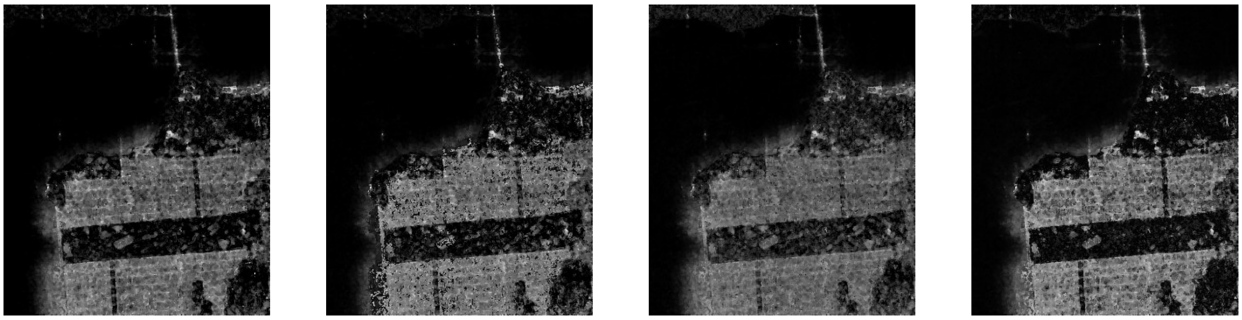
（a）FDD （b）Y4D （c）7SD （d）PD

Fig. 7 Double-bounce scattering power of the coherency matrix
图7 相干矩阵的二次散射能量

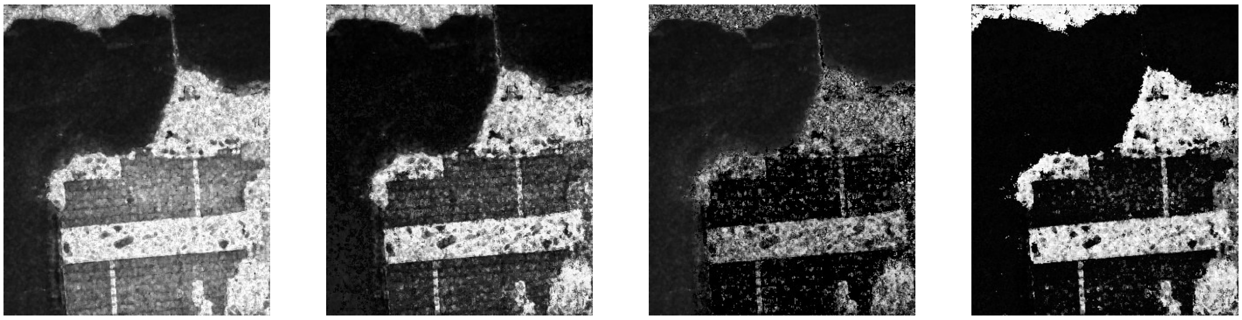
（a）FDD （b）Y4D （c）7SD （d）PD

Fig. 8 Volume scattering power of the coherency matrix
图8 相干矩阵的体散射能量

zone2，PD algorithm has the highest proportion of double-bounce scattering power，while 7SD algorithm focuses its power on double-bounce scattering，mixed dipole scattering and surface scattering. PD algorithm concentrates its power on double-bounce scattering，surface scattering，and mixed dipole scattering sequentially. This phenomenon is consistent with the possible scattering types that may occur in urban areas. In zone3，PD algorithm obtains the highest volume scattering power，accounting for as much as 90.41%. Because the PD algorithm has been improved using entropy to decompose the coherency matrix. If entropy $H$ is high and anisotropy $A$ is low，i. e.，$H - A > 0.4$，it considers that surface scattering does not exist，and the scattering power with scattering angle less than 50° is classified as volume scattering，which increases the volume scattering power.

The scattering power from these decomposition algorithms for the coherency matrices with OAC by using $R(\theta)$ in zone1，zone2，and zone3 is displayed in Tables 4-6，respectively. Because after OAC $R(\theta)$，$m_{md} = 0$，so PD and 7SD both have six scattering power. In zone1 (shown in Table 4)，the proportion of surface scattering power of PD algorithm is as high as 93.96%，only slightly inferior to Y4D. These four algorithms obtain a higher proportion of surface scattering power than 92%. In zone2 (shown in Table 5)，the double-bounce scattering

**Table 1 Scattering power in zone1 for $\langle T \rangle$ (%)**
**表1 相干矩阵*T*区域1的散射能量(%)**

| Method<br>Powers | FDD | Y4D | 7SD | PD |
|---|---|---|---|---|
| $m_s$ | 91.62 | 94.21 | 91.85 | 93.64 |
| $m_d$ | 0.01 | 0.18 | 0.25 | 0.95 |
| $m_v$ | 8.36 | 3.02 | 7.91 | 2.60 |
| $m_h$ | —— | 2.59 | 0 | 0.28 |
| $m_{md}$ | —— | —— | 0 | 0.10 |
| $m_{od}$ | —— | —— | 0 | 1.16 |
| $m_{cd}$ | —— | —— | 0 | 1.26 |

**Table 2 Scattering power in zone2 for $\langle T \rangle$ (%)**
**表2 相干矩阵*T*区域2的散射能量(%)**

| Method<br>Powers | FDD | Y4D | 7SD | PD |
|---|---|---|---|---|
| $m_s$ | 13.21 | 30.41 | 25.81 | 32.90 |
| $m_d$ | 35.41 | 37.82 | 32.75 | 40.51 |
| $m_v$ | 51.38 | 26.50 | 6.51 | 7.03 |
| $m_h$ | —— | 5.27 | 3.59 | 1.95 |
| $m_{md}$ | —— | —— | 18.36 | 8.98 |
| $m_{od}$ | —— | —— | 9.98 | 5.78 |
| $m_{cd}$ | —— | —— | 3.02 | 2.85 |

**Table 3 Scattering power in zone3 for $\langle T \rangle$ (%)**
**表3 相干矩阵$T$区域3的散射能量(%)**

| Method Powers | FDD | Y4D | 7SD | PD |
|---|---|---|---|---|
| $m_s$ | 3.15 | 7.09 | 15.97 | 2.96 |
| $m_d$ | 7.07 | 9.14 | 15.17 | 6.53 |
| $m_v$ | 89.77 | 79.12 | 44.92 | 90.41 |
| $m_h$ | —— | 4.65 | 4.46 | 0.02 |
| $m_{md}$ | —— | —— | 5.38 | 0.02 |
| $m_{od}$ | —— | —— | 7.11 | 0.02 |
| $m_{cd}$ | —— | —— | 6.99 | 0.04 |

power of PD algorithm is the highest one, and it is 50.06%. In zone3 (shown in Table 6), PD algorithm gets the highest volume scattering power, which is 88.58%. It is 1.51%, 14.89% and 40.32% higher than FDD, Y4D and 7SD respectively.

**Table 4 Scattering power in zone1 for $\langle T(\theta) \rangle$ (%)**
**表4 相干矩阵$T(\theta)$区域1的散射能量(%)**

| Method Powers | FDD | Y4D | 7SD | PD |
|---|---|---|---|---|
| $m_s$ | 92.07 | 94.67 | 92.26 | 93.96 |
| $m_d$ | 0.07 | 0.15 | 0.29 | 1.00 |
| $m_v$ | 7.91 | 2.61 | 7.44 | 2.34 |
| $m_h$ | —— | 2.57 | 0 | 0.34 |
| $m_{od}$ | —— | —— | 0 | 0.64 |
| $m_{cd}$ | —— | —— | 0 | 1.73 |

**Table 5 Scattering power in zone2 for $\langle T(\theta) \rangle$ (%)**
**表5 相干矩阵$T(\theta)$区域2的散射能量(%)**

| Method Powers | FDD | Y4D | 7SD | PD |
|---|---|---|---|---|
| $m_s$ | 19.58 | 34.61 | 28.45 | 31.04 |
| $m_d$ | 43.35 | 43.37 | 47.51 | 50.06 |
| $m_v$ | 37.08 | 17.03 | 3.39 | 4.89 |
| $m_h$ | —— | 4.99 | 4.80 | 2.80 |
| $m_{od}$ | —— | —— | 10.14 | 7.27 |
| $m_{cd}$ | —— | —— | 5.71 | 3.94 |

**Table 6 Scattering power in zone3 for $\langle T(\theta) \rangle$ (%)**
**表6 相干矩阵$T(\theta)$区域3的散射能量(%)**

| Method Powers | FDD | Y4D | 7SD | PD |
|---|---|---|---|---|
| $m_s$ | 3.79 | 9.06 | 13.58 | 4.49 |
| $m_d$ | 10.14 | 12.60 | 19.46 | 6.84 |
| $m_v$ | 86.07 | 73.69 | 48.26 | 88.58 |
| $m_h$ | —— | 4.65 | 4.59 | 0.02 |
| $m_{od}$ | —— | —— | 7.83 | 0.02 |
| $m_{cd}$ | —— | —— | 6.29 | 0.05 |

The scattering power from these decomposition algorithms for the coherency matrices with two types of OAC by using $R(\theta)$ and $U(\varphi)$ successively in zone1, zone2, and zone3 is displayed in Tables 7-9, respectively. Because after OAC by $R(\theta)$ and $U(\varphi)$, $m_{md} = 0$ and $m_h = 0$, PD and 7SD both have five scattering power. In zone1 (shown in Table 7), the proportion of surface scattering power of PD is as high as 95.17%, only slightly inferior to FDD. These four algorithms obtain a higher proportion of surface scattering power than 93%. Compared with Table 4, double-bounce scatting power shows a slight improvement. In zone2 (shown in Table 8), the double-bounce scattering power of PD is the highest one, at 51.77%. In zone3 (shown in Table 9), PD obtains the highest volume scattering power, which is 87.30%. This is 3.77%, 10.21% and 32.44% higher than FDD, Y4D and 7SD respectively. Compared with Table 6 and Table 3, although there is a slight decrease in volume scattering in Table 9, the volume scattering still occupies an absolute dominant position.

**Table 7 Scattering power in zone1 for $\langle T(\varphi) \rangle$ (%)**
**表7 相干矩阵$T(\varphi)$区域1的散射能量(%)**

| Method Powers | FDD | Y4D | 7SD | PD |
|---|---|---|---|---|
| $m_s$ | 94.08 | 93.95 | 94.52 | 95.17 |
| $m_d$ | 0.19 | 0.67 | 1.01 | 1.33 |
| $m_v$ | 5.74 | 5.38 | 3.45 | 1.34 |
| $m_{od}$ | —— | —— | 0.62 | 1.33 |
| $m_{cd}$ | —— | —— | 0.41 | 0.82 |

**Table 8 Scattering power in zone2 for $\langle T(\varphi) \rangle$ (%)**
**表8 相干矩阵$T(\varphi)$区域2的散射能量(%)**

| Method Powers | FDD | Y4D | 7SD | PD |
|---|---|---|---|---|
| $m_s$ | 20.15 | 32.73 | 29.26 | 30.04 |
| $m_d$ | 43.93 | 45.83 | 50.19 | 51.77 |
| $m_v$ | 35.92 | 21.44 | 4.62 | 5.23 |
| $m_{od}$ | —— | —— | 10.11 | 8.36 |
| $m_{cd}$ | —— | —— | 5.81 | 4.60 |

**Table 9 Scattering power in zone3 for $\langle T(\varphi) \rangle$ (%)**
**表9 相干矩阵$T(\varphi)$区域3的散射能量(%)**

| Method Powers | FDD | Y4D | 7SD | PD |
|---|---|---|---|---|
| $m_s$ | 4.34 | 8.05 | 10.55 | 5.31 |
| $m_d$ | 12.13 | 14.86 | 21.01 | 7.31 |
| $m_v$ | 83.53 | 77.09 | 54.86 | 87.30 |
| $m_{od}$ | —— | —— | 7.29 | 0.02 |
| $m_{cd}$ | —— | —— | 6.29 | 0.05 |

## 3 Conclusions

This letter proposes a modified multiple-component scattering power decomposition. This proposed algorithm combines eigenvalue decomposition with model decomposition. Referring to 7SD[9], this letter employs seven scattering models. Entropy and anisotropy are utilized to estimate the volume scattering power. The effectiveness of the proposed algorithm is demonstrated by experiments conducted on real PolSAR data, particularly in vegetation areas.

## References

[1] A. Freeman, S. L. Durden. A three-component scattering model for polarimetric SAR data [J]. *IEEE Transactions on geoscience and remote sensing*, 1998, **36**(3): 963-973.

[2] XU Feng, JIN Ya-Qiu. Deorientation theory of polarimetric scattering targets and application to terrain surface classification [J]. *IEEE Transactions on geoscience and remote sensing*, 2005, **43**(10): 2351-2364.

[3] Y. Yamaguchi, A. Sato, W. M. Boerner, *et al*. Four-component scattering power decomposition with rotation of coherency matrix [J]. *IEEE Transactions on geoscience and remote sensing*, 2011, **49**(6): 2251-2258.

[4] G. Singh, Y. Yamaguchi, S. E. Park. General four-component scattering power decomposition with unitary transformation of coherency matrix [J]. *IEEE Transactions on geoscience and remote sensing*, 2013, **51**(5): 3014-3022.

[5] Y. Yamaguchi, T. Moriyama, M. Ishido, *et al*. Four-component scattering model for polarimetric SAR image decomposition [J]. *IEEE Transactions on Geoscience and Remote Sensing*, 2005, **43**(8): 1699-1706.

[6] A. Sato, Y. Yamaguchi, G. Singh, *et al*. Four-component scattering power decomposition with extended volume scattering model [J]. *IEEE Geoscience and Remote Sensing Letters*, 2012, **9**(2): 166-170.

[7] ZHANG La-Mei, ZOU Bin, CAI Hong-Jun, *et al*. Multiple-component scattering model for polarimetric SAR image decomposition [J]. *IEEE Geoscience and Remote Sensing Letters*, 2008, **5**(4): 603-607.

[8] G. Singh, Y. Yamaguchi. Model-based six-component scattering matrix power decomposition [J]. *IEEE Transactions on Geoscience and Remote Sensing*, 2018, (56)10: 5687-5704.

[9] G. Singh, R. Malik, S. Mohanty, *et al*. Seven-component scattering power decomposition of POLSAR coherency matrix [J]. *IEEE Transactions on Geoscience and Remote Sensing*, 2019, **57**(11): 8371-8382.

[10] AN Wen-Tao, LIN Ming-Sen, YANG Hai-Jun. Modified reflection symmetry decomposition and a new polarimetric product of GF-3 [J]. *IEEE Geoscience and Remote Sensing Letters*, 2022, **19**: 8019805.

[11] LI Hong-Zhong, LI Qing-Quan, WU Guo-Feng, *et al*. Adaptive two-component model-based decomposition for polarimetric SAR data without assumption of reflection symmetry [J]. *IEEE Transactions on Geoscience and Remote Sensing*, 2017, **55**(1): 197-211.

[12] XIANG De-Lin, WANG Wei, TANG Tao, *et al*. Multiple-component polarimetric decomposition with new volume scattering models for PolSAR urban areas [J]. *IET Radar, Sonar & Navigation*, 2017, **11**(3): 410-419.

[13] V. Turkar, J. Checker, S. De. Impact of G4U and 7-component target decomposition on PolSAR image semantic segmentation [J]. *Advances in Space Research*, 2022, **70**(12): 3798-3810.

[14] HAN Wen-Tao, FU Hai-Qiang, ZHU Jian-Jun, *et al*. Polarimetric SAR decomposition by incorporating a rotated dihedral scattering model [J]. *IEEE Geoscience and Remote Sensing Letters*, 2022, **19**: 4005505.

[15] S. R. Cloude, E. Pottier. An entropy based classification scheme for land applications of polarimetric SAR [J]. *IEEE Transactions on Geoscience and Remote Sensing*, 1997, **35**(1): 68-78.

[16] S. R. Cloude. Polarisation: Applications in Remote Sensing [M]. London, U.K.: Oxford Univ. Press, 2009.

[17] G. Singh, Y. Yamaguchi, S. E. Park. Hybrid Freeman/eigenvalue decomposition method with extended volume scattering model [J]. *IEEE Geoscience Remote Sensing Letters*, 2013, **10**(1): 81-83.

[18] SUN Bo-Rong, TAN Wei-Xian, XU Wei. An improved hybrid Freeman/eigenvalue decomposition for polarimetric SAR data [C]. 2019 IEEE International Conference on Signal, Information and Data Processing (ICSIDP), 2019: 19892107.

[19] ZHANG Shuang, YU Xiang-Chuan, WANG Lu. Modified version of three-component model-based decomposition for polarimetric SAR data [J]. *Journal of Systems Engineering and Electronics*, 2019, **30**(2): 270-277.

[20] G. Singh, Y. Yamaguchi, S. E. Park. Generalized hybrid model-based/eigenvalue decomposition [C]. 2013 Asia-Pacific Conference on Synthetic Aperture Radar (APSAR), 2013: 14026506.

[21] J.-J. van Zyl, Y. Kim, M. Arii. Requirements for model-based polarimetric Decompositions [C]. 2008 IEEE International Geoscience and Remote Sensing Symposium (IGARSS), 2008: 10472722.

[22] J. J. van Zyl, M. Arii, Y. Kim. Model-Based decomposition of polarimetric SAR covariance matrices constrained for nonnegative eigenvalues [J]. *IEEE Transactions on Geoscience and Remote Sensing*, 2011, **49**(9): 3452-3459.